minerals

MDPI

Article

Kinematics and Dynamics Behaviour of Milling Media in Vertical Spiral Stirred Mill Based on DEM-CFD Coupling

Ruijie Gu [1,2], Wenzhe Wu [1], Shuaifeng Zhao [1,*], Zhenyu Ma [1], Qiang Wang [1], Zhenzhong Qin [1] and Yan Wang [2]

[1] School of Mechatronics Engineering, Henan University of Science and Technology, Luoyang 471003, China; 9906625@haust.edu.cn
[2] State Key Laboratory of Intelligent Mining Heavy Equipment, Luoyang 471003, China
* Correspondence: zsf588@haust.edu.cn

Abstract

The kinematic and dynamic characteristics of the grinding media during the wet grinding process are investigated using a coupled Discrete Element Method (DEM)–Computational Fluid Dynamics (CFD) approach. Firstly, a coupled DEM-CFD model of the vertical spiral agitator mill is established and validated with experimental torque measurements. Subsequently, a velocity analysis model is established using the vector decomposition method. The cylinder is then divided into multiple regions along its radial and axial directions. The effects of spiral agitator rotational speed, diameter, pitch, and media filling level are investigated with respect to the circumferential velocity, axial velocity, collision frequency, effective energy between media, and energy loss of the grinding media. The average effective energy between media is an innovative metric for evaluating the grinding effect. The results indicate that the peripheral region of the spiral agitator demonstrates superior kinematic and dynamic performance. The rotational speed of the spiral agitator exerts a highly significant influence on the kinematic and dynamic characteristics of the media. With a maximum rise of 0.2 m/s in circumferential velocity and a 16.7 J gain in total energy. The media filling level demonstrates a negligible influence on media kinematics, while it profoundly affects dynamic properties, evidenced by a substantial increase of 83.09 J in the total media–media energy. As the diameter increases, the peak media circumferential velocity shifts outward, and the total media–media energy rises by 5.4 J. The spiral agitator pitch has a minimal impact on both the kinematic and dynamic characteristics of the media.

Keywords: vertical spiral agitator mill; DEM-CFD coupling; kinetic analysis; dynamic characteristics

Check for updates

Academic Editor: Rodrigo Magalhães de Carvalho

Received: 29 November 2025
Revised: 18 December 2025
Accepted: 23 December 2025
Published: 24 December 2025

Copyright: © 2025 by the authors. Licensee MDPI, Basel, Switzerland. This article is an open access article distributed under the terms and conditions of the Creative Commons Attribution (CC BY) license.

1. Introduction

Sustainable development in mineral processing urgently requires a breakthrough in the energy-intensive nature of fine grinding [1,2]. This is particularly critical as the comminution stage currently represents more than 50% of the total energy consumption in mineral processing plants. The vertical spiral agitator mill, recognised as a core unit in ultra-fine grinding for its high efficiency, low energy use, and consistent product size [3,4], is consequently widely employed in applications ranging from metal ore regrinding to ultra-fine processing of non-metallic minerals. The structure of the vertical spiral agitator mill is composed of the main frame, drive assembly, grinding chamber, and the spiral agitator [5,6]. The working principle of a vertical spiral stirred mill involves grinding

materials primarily through friction, shearing, and compression, with a minor contribution from impact, with the process schematic provided in Figure 1 [7].



Figure 1. Comminution mechanism in the vertical spiral agitator mill.

The wet grinding process within a vertical spiral agitator mill is a coupled solid–liquid-mechanical system. The kinematic state and dynamic behaviour of the grinding media serve as the core physical mechanism governing both efficiency and energy consumption, by directly determining the efficacy of mechanical energy conversion, the probability and intensity of mineral breakage, and the energy loss from non-breaking collisions [8]. Consequently, an in-depth understanding and analysis of the media's kinematics and dynamics inside the mill chamber form the theoretical cornerstone for the optimisation of equipment design, operational strategies, and the grinding process itself [9].

The DEM, recognised for its unique capability in modelling granular or discontinuous materials, has become an essential tool in rock mechanics, mining, and energy engineering. This has led to its widespread adoption by researchers for investigating vertical stirred mills [10–12]. Fukui et al. [13], through comparative experimental and DEM simulation studies, found that horizontal shaft stirrer mills outperform vertical designs due to their more uniform media motion and consistent energy transfer, resulting in superior grinding performance. Osborne, T. et al. [14] employed the DEM to investigate the design of a pin mill by varying the number of pins and their projected region under different rotational speeds. Their analysis revealed that the addition of pins enhanced its effective grinding capacity. Daraio, D. et al. [15] employed the Coarse-Graining (CG) technique on DEM-derived data of media motion within a vertical stirred mill to reconstruct continuum fields, which quantitatively delineated the spatial distributions of solid fraction, kinetic energy, and static pressure for two impeller arm lengths at both low and high rotational speeds. D. Rhymer et al. [16] studied the influence of the coefficients of restitution and sliding friction among grinding media on the grinding efficiency in vertical stirred mills. A key finding was that a reduction in the sliding friction coefficient below 0.1 led to significant changes across the parameter space. Subsequently, DEM simulations by D. Rhymer et al. [17] revealed that mixing grinding media of different sizes not only increased the effective energy between media to enhance grinding efficiency but also reduced energy consumption.

Conventional numerical models, such as single-phase CFD [18] or independent DEM, had obvious limitations in capturing the key coupling effects between fluid turbulence and discrete particle behaviour [19]. Consequently, a growing number of researchers are turning to the development of coupled multiphysics models to more accurately simulate the complex dynamics within vertical stirred mills during wet grinding processes [20]. Fragnière, G. et al. [21] employed a coupled DEM-CFD approach to analyse grinding media motion within a stirred mill. Their study revealed significant variations in collision frequency distribution under different filling levels and rotational speeds. Ji, H. et al. [22] developed a DEM-CFD model of an experimental vertical stirred mill and systematically analysed grinding media motion in terms of trajectory, velocity, force, and energy. Their

analysis identified five distinct grinding zones, which revealed varying functional contributions across different regions. The observed motion characteristics provided deeper insights into the underlying comminution mechanism. Ford, E. et al. [23] demonstrated through comparative experiments that incorporating a stationary disc liner into the shell of a vertical fluidised stirred mill significantly increased power consumption and silica grinding throughput, without compromising energy efficiency. Although numerous studies have focused on the wet grinding process in vertical stirred mills [24–26], research remains limited regarding how structural and operational parameters affect the kinematic state and dynamic characteristics of the grinding media.

In summary, the investigation focuses on the kinematic and dynamic characteristics of grinding media inside a vertical spiral stirrer mill. A numerical model of the vertical spiral stirrer mill is established based on the DEM-CFD coupling approach and experimental validation. To facilitate analysis, a velocity analysis model is established using the vector decomposition method. The cylinder is subdivided into multiple regions along the radial and axial directions. Furthermore, the effects of rotational speed, diameter, pitch, and filling level on the circumferential and axial velocity distribution, collision frequency, effective energy between media, and energy loss of the grinding media are investigated. The findings presented serve as a key theoretical foundation for optimising both the structural design and operational parameters of the mill, guiding the pathway toward enhanced grinding efficiency.

2. Materials and Methods

The wet grinding process in a vertical spiral stirrer mill was simulated using a coupled DEM-CFD approach. The Hertz–Mindlin (no-slip) contact model was employed to characterise the elastic compression, microscopic slip, and rolling behaviour of particles within the high-concentration slurry. The fluid phase was described by the Navier–Stokes equations, with the solid–liquid interaction dominated by the drag force. The simulation employed a dynamic mesh to handle the spiral agitator rotation and adopted the SST turbulence model. Simulation experiments were designed with variables including rotational speed, diameter, pitch, and filling level, and the reliability of the model was verified through comparison with experimental data.

2.1. Contact Model

The contact model is employed to characterise the mechanical interactions between discrete ore particles, or between particles and geometric boundaries, in EDEM simulations. Its core mechanism utilises physical equations to simulate phenomena such as collision, friction, and bonding [27]. The Hertz–Mindlin (no-slip) contact model is widely employed in simulating the grinding process within the vertical spiral stirrer mill, as illustrated in Figure 2 [28,29]. Within the high-concentration slurry of a stirrer mill, macroscopic sliding between particles is restricted, and the dominant contact mechanisms are dominated by elastic compression, microscopic slip, and rolling [30]. By enforcing the condition that the tangential force cannot exceed the Coulomb friction limit ($Ft \leq \mu Fn$), this model naturally captures the physical scenario dominated by static friction. This behaviour aligns more closely with the actual kinematics and dynamics of grinding media and fine-particle slurry within a confined space. Thus, Hertz–Mindlin (no-slip) is selected as the contact model in this work.

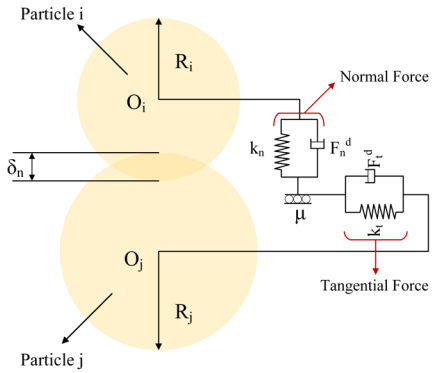


Figure 2. Hertz–Mindlin (no-slip) contact model.

In this model, the normal force component is modelled based on Hertzian contact theory, where the normal force F_n (N) is defined as a function of the normal overlap δ_n (m), the equivalent Young's modulus E^* (Pa) and equivalent radius R^* (m) are defined as in Equation (1),

$$F_n = \frac{4}{3} E^* \sqrt{R^*} \delta_n^{\frac{3}{2}} \tag{1}$$

$$\frac{1}{E^*} = \frac{\left(1-v_i^2\right)}{E_i} + \frac{\left(1-v_j^2\right)}{E_j} \tag{2}$$

$$\frac{1}{R^*} = \frac{1}{R_i} + \frac{1}{R_j} \tag{3}$$

where E_i (Pa), V_i, R_i (m) and E_j (Pa), V_j, R_j (m) represent the Young's modulus, Poisson's ratio, and radius of the two contacting spheres, respectively. Additionally, a damping force F_n^d (N) acts on the spheres during contact, which is expressed by,

$$F_n^d = -2\sqrt{\frac{5}{6}} \beta \sqrt{c_n m^*} \vec{v_n} \tag{4}$$

where $m^* = \left(\frac{1}{m_i} + \frac{1}{m_j}\right)^{-1}$ (kg) represents the equivalent mass, in Equation (4), and $\vec{v_n}$ (m/s) denotes the normal relative velocity. The parameter β and the normal stiffness c_n (N/m) are defined as follows,

$$\beta = \frac{-lne}{\sqrt{ln^2 e + \pi^2}} \tag{5}$$

$$c_t = 8G^* \sqrt{R^* \delta_n} \tag{6}$$

where e denotes the coefficient of restitution.

The tangential force model draws on the work of Mindlin–Deresiewicz, where the tangential force F_t (N) depends on the tangential overlap c_t (m) and the tangential stiffness δ_t (N/m), and is given by,

$$F_t = -c_t \delta_t \tag{7}$$

$$c_t = 8G^* \sqrt{R^* \delta_n} \tag{8}$$

where G^* (Pa) represents the equivalent shear modulus, and the tangential damping force F_t^d (N) is defined as,

$$F_t^d = -2\sqrt{\frac{5}{6}} \beta \sqrt{c_t m^*} \vec{v_t} \tag{9}$$

where $\vec{v_t}$ (m/s) is the tangential relative velocity. The tangential force is also influenced by Coulomb friction μF_n.

2.2. DEM-CFD Coupling Model

The vertical spiral agitator mill experiences dynamic variations in its transient performance during wet grinding, accompanied by slurry fluctuations and media collisions. However, wet grinding is the predominant method in practical engineering applications [31]. Consequently, the present investigation develops a simulation model for the wet grinding process in a vertical spiral stirrer mill using a DEM-CFD approach, with the schematic diagram of the methodology presented in Figure 3.

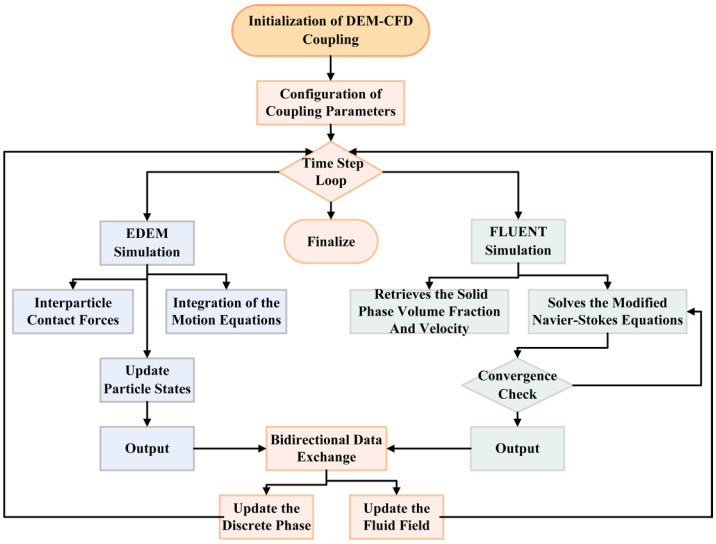


Figure 3. The coupling principle diagram of DEM-CFD.

The Eulerian–Eulerian approach is employed for the solid–liquid two-phase coupling calculations. The motion of the liquid slurry is governed by the Navier–Stokes equations [32]. The continuity equation for the liquid phase is given by Equation (10):

$$\frac{\partial(\alpha_f \rho_f)}{\partial_t} + \nabla \cdot \left(\alpha_f \rho_f \mu_f\right) = 0 \tag{10}$$

where α_f, ρ_f (kg/m^3), μ_f (m/s) represent the liquid phase volume fraction, density, and velocity vector, respectively. The momentum equation for the liquid phase is given by Equation (11):

$$\frac{\partial(\alpha_f \rho_f \mu_f)}{\partial_t} + \nabla \cdot \left(\alpha_f \rho_f \mu_f \mu_f\right) = -\alpha_f \nabla_p + \nabla \cdot \left(\alpha_f \tau_f\right) + \alpha_f \rho_f g - F_{coupling} \tag{11}$$

where τ_f (Pa) is the viscous stress tensor of the liquid phase, g (m/s^2) denotes the gravitational acceleration, and $F_{coupling}$ (N) represents the solid–liquid coupling force, which accounts for the resistance exerted by the solid particles on the fluid. The drag force constitutes the dominant component in this coupling force and is expressed as:

$$F_{drag} = \frac{3}{4} C_d \frac{\alpha_s \alpha_f \rho_f}{d_p} \left|\mu_f - \mu_s\right| \left(\mu_f - \mu_s\right) \tag{12}$$

where C_d denotes the drag coefficient, α_s the solid phase volume fraction, and μ_s (m/s) the solid phase velocity vector.

2.3. Simulation Model

A simplified version of a vertical spiral stirrer mill was employed to simulate the wet grinding process. The three-dimensional model of the mill was constructed and subsequently imported into Fluent Flow for dynamic mesh generation, as illustrated in Figure 4.

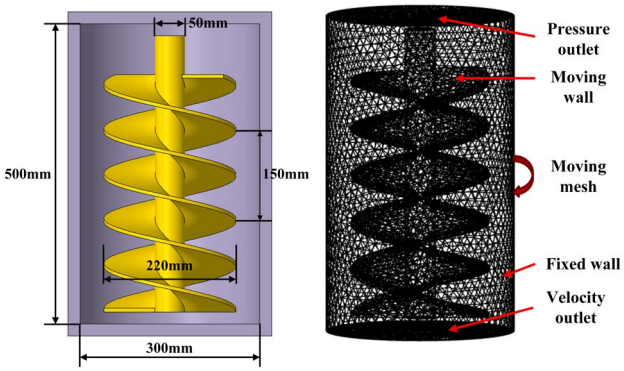


Figure 4. Three-dimensional model and dynamic mesh of the vertical spiral stirred mill.

The internal boundaries of the fluid domain exhibit significant temporal variation due to the persistent rotational motion of the spiral agitator. The dynamic mesh technique typically combines the Layering Method, Elastic Smoothing, and Local Remeshing to efficiently and robustly handle rotational motion. Therefore, to accurately simulate the complex interactions between the spiral agitator and the surrounding slurry, the dynamic mesh approach was employed to model the shaft's rotation. Since the agitator rotated synchronously with the mesh in its surrounding rotating domain, the relative velocity between the agitator wall and the adjacent fluid mesh was zero. The mill cylinder wall remained stationary, and thus a no-slip boundary condition was enforced. The mesh generation followed FLUENT's solver-specific preferences. To prevent numerical divergence resulting from mesh cells being significantly smaller than the particle volume, a minimum mesh size of 15 mm was enforced throughout the computational domain [33,34].

The discrete element method software EDEM (2023) was employed for the DEM-CFD coupling simulations. The rotational speed of the spiral agitator in EDEM was set to be consistent with the value defined in ANSYS Fluent (19.2). The grinding media, mill cylinder, and spiral agitator were modelled as rigid bodies. The grinding media consisted of spherical particles with a diameter of 12 mm. The contact parameters and material properties for both the media and the mill components are provided in Table 1 [35]. When configuring the time steps, the data exchange between the solvers was synchronised. Accordingly, the time step in Fluent was typically set to 1–100 times that used in EDEM [36,37]. The total simulation time was 6 s.

Table 1. Material and contact parameters used in DEM simulations.

Setting	Parameters	Values	Values
DEM settings	Individual parameters	Ball	Mill
	Density	7800 kg/m^3	7800 kg/m^3
	Shear stiffness	7×10^{10} pa	7×10^{10} pa
	Poisson's ratio	0.3	0.3
	Contact parameters	Ball-ball	Ball-mill
	Coefficient of restitution	0.1	0.1
	Coefficient of static friction	0.5	0.5
	Coefficient of rolling friction	0.1	0.1

The SST k-ω model was selected for turbulence closure in the simulation [38]. For the discretisation schemes, the Second Order Upwind method was employed for momentum, turbulent kinetic energy, and turbulent dissipation rate, while the First Order Upwind scheme was used for the volume fraction.

2.4. Experimental Verification

Tie Qu et al. [39] developed a DEM-CFD approach to address the complexity of solid–liquid two-phase flow dynamics within a vertical spiral stirrer mill, validating the numerical model against experimental measurements. The outer diameter, height and wall thickness of the cylinder of the test prototype were 300 mm, 500 mm, 20 mm, respectively. The spiral agitator has a diameter of 220 mm. In the experiment, the grinding tests were conducted using Longmang iron concentrate as the feed material, with its chemical composition detailed in Table 2. The feed had a particle size distribution where more than 50% passed 200 mesh, and the maximum particle size was below 300 μm [40]. A total of 11.2 kg of the concentrate was thoroughly mixed with water and then fed into the test machine. The operational parameters are summarised in Table 3.

Table 2. Chemical Composition of Longmang Iron Concentrate.

Composition	TFe	FeO	SiO_2	MgO	Al_2O_3	CaO	P	S
Percentage	33.42	4.81	46.92	0.49	0.86	0.56	0.043	0.026

Table 3. Operating Parameters of the Experimental Prototype.

Parameters	Spiral Agitator Rotational Speed (rpm)	Media Filling Mass (kg)	Grinding Media Diameter (mm)	Stirring Spiral Angle (°)	Slurry Solid Concentration (%)	Slurry Density (kg/m^3)
Values	175	49	8	14.21	62.5	1957.4

The average torque over the stable operation period was taken as the experimental value, which was measured to be 16.22 N·m. To validate the reliability of the developed fluid-particle coupled simulation model, the dimensions and operational parameters of the aforementioned experimental setup were adopted together with the boundary conditions listed in Table 1. Multiple simulation runs were conducted and compared with the experimental results reported by Qu et al. [39], as summarised in Table 4. The maximum discrepancy was 3.4%, which remained below the 5% threshold, indicating that the observed error fell within an acceptable range.

Table 4. Experimental Torque Results.

Simulation Results	15.66	15.69	15.71
Error	3.4%	3.27%	3.14%

2.5. Design of Simulation Experiments

The kinematic state and dynamic behaviour of the media within the vertical spiral stirrer mill are strongly influenced by multiple factors, including the spiral agitator geometry, operational parameters, and material properties. This study investigates the influence of key operational factors, including the spiral agitator rotational speed, diameter, pitch, and the media filling level, on the kinematics and dynamics of the grinding media. Under actual operating conditions, the parameters of a vertical spiral stirrer mill are maintained within specific ranges. For instance, excessively high agitator rotational speed can lead to an oversized axial lifting force, causing media suspension and excessive

centrifugal forces that result in the accumulation of grinding media near the chamber wall and a reduction in the effective grinding zone. This not only increases energy dissipation but also accelerates agitator wear, thereby shortening equipment service life. Accordingly, comprehensive considerations including the specifications of the available laboratory prototype and computational efficiency led to the experimental layout presented in Table 5. The total simulation time was 6 s. The parameters analyzed in this work are based on data collected during stable operation and represent mean values from that period. The experimental prototype is shown in Figure 5. The following parameters were set as standard values: spiral agitator rotational speed of 80 rpm, spiral agitator diameter of 220 mm, spiral agitator pitch of 150 mm, and media filling level of 40%. At rotational speeds of 80, 90, 100, 110, and 120 rpm, the resulting tip velocities of the spiral agitator are 0.92, 1.04, 1.15, 1.27, and 1.38 m/s, respectively.

Table 5. Parameters of simulation models at different levels.

Factors	1	2	3	4	5
Spiral agitator rotational speed (rpm)	80	90	100	110	120
Spiral agitator diameter (mm)	200	205	210	215	220
Spiral agitator pitch (mm)	150	160	170	180	190
Media filling level (%)	30	35	40	45	50

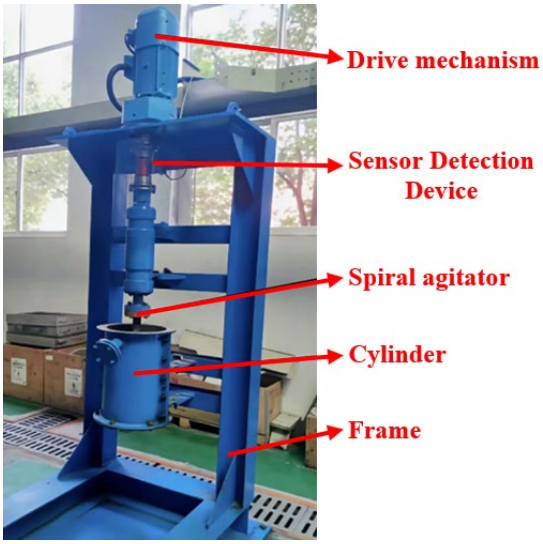


Figure 5. Experimental prototype.

The velocity analysis model was established using the vector decomposition method to analyse the circumferential velocity (*c*-direction), axial velocity (*z*-direction), and radial velocity (*r*-direction). To investigate the kinematic and dynamic behaviour of the grinding media in different sections of the mill chamber, the chamber was partitioned into sequential intervals along the radial and axial directions, as shown in Figure 6a,b. The radial zones are spaced at 12.5 mm intervals. Zones S_1–S_7 constitute the spiral agitator, with S_6 and S_7 located at the edge of the spiral agitator. Zones S_8–S_{10} correspond to the circulation region. Axially, L_1 defines the bottom clearance with a height of 20 mm, while zones L_2–L_9 are equally spaced along the axial direction at intervals of 35 mm.

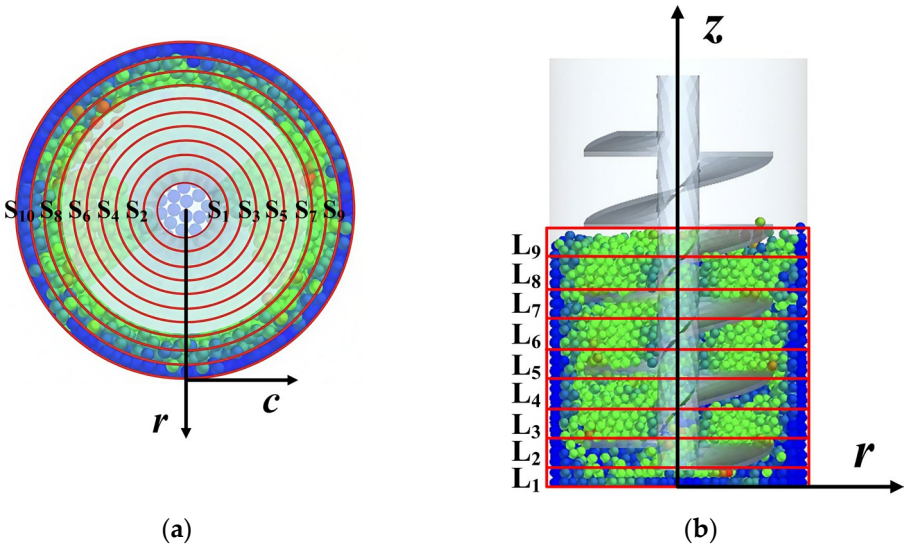


Figure 6. Velocity direction model of the grinding media: (**a**) Radial zoning of the mill chamber; (**b**) Axial zoning of the mill chamber.

3. Results and Analyses

Based on the aforementioned research conditions and methodology, the kinematic and dynamic characteristics of the grinding media during the grinding process in the vertical spiral agitator mill were investigated and calculated. Furthermore, the grinding effect under various factors is investigated by employing the effective energy between grinding media as the evaluation metric.

3.1. Effect of Rotational Speed on Media Kinematics and Dynamics

The grinding media exhibits distinct motion characteristics across different regions of the mill chamber. Figure 7 illustrates the influence of rotational speed on the velocity distribution of the media. The curves for regions near the spiral agitator axis (S_1–S_3) display a nearly linear increasing trend under all rotational speed conditions, as shown in Figure 7a. With increasing radial position, the curve slope progressively decreases, corresponding to a reduced velocity growth rate that attains its maximum value of 0.495 m/s in Zone S_6. The velocity in the circulation region subsequently shows a clear decaying trend. This finding is consistent with previous literature [14,21]. As predicted by Goodson et al., regarding the velocity distribution pattern, the location of the maximum velocity is independent of the rotational speed but is determined by the design of the spiral agitator [15]. The circumferential velocity of the media first increases and then decreases along the radial direction. The resulting velocity gradient generates intense inter-layer shear forces; the greater the velocity difference, the stronger the shear action, which enhances the fine grinding process. Within the mill chamber, the relative sliding and compression of the grinding media exert shear and compressive forces on the material, thereby achieving efficient grinding [41,42]. When the rotational speed increases from 80 to 120 rpm, the circumferential velocity of the grinding media rises by 0.2 m/s in the S_6 region, with a nearly proportional increase observed across all zones. This demonstrates a positive correlation between the circumferential velocity of the grinding media and the rotational speed of the spiral agitator.

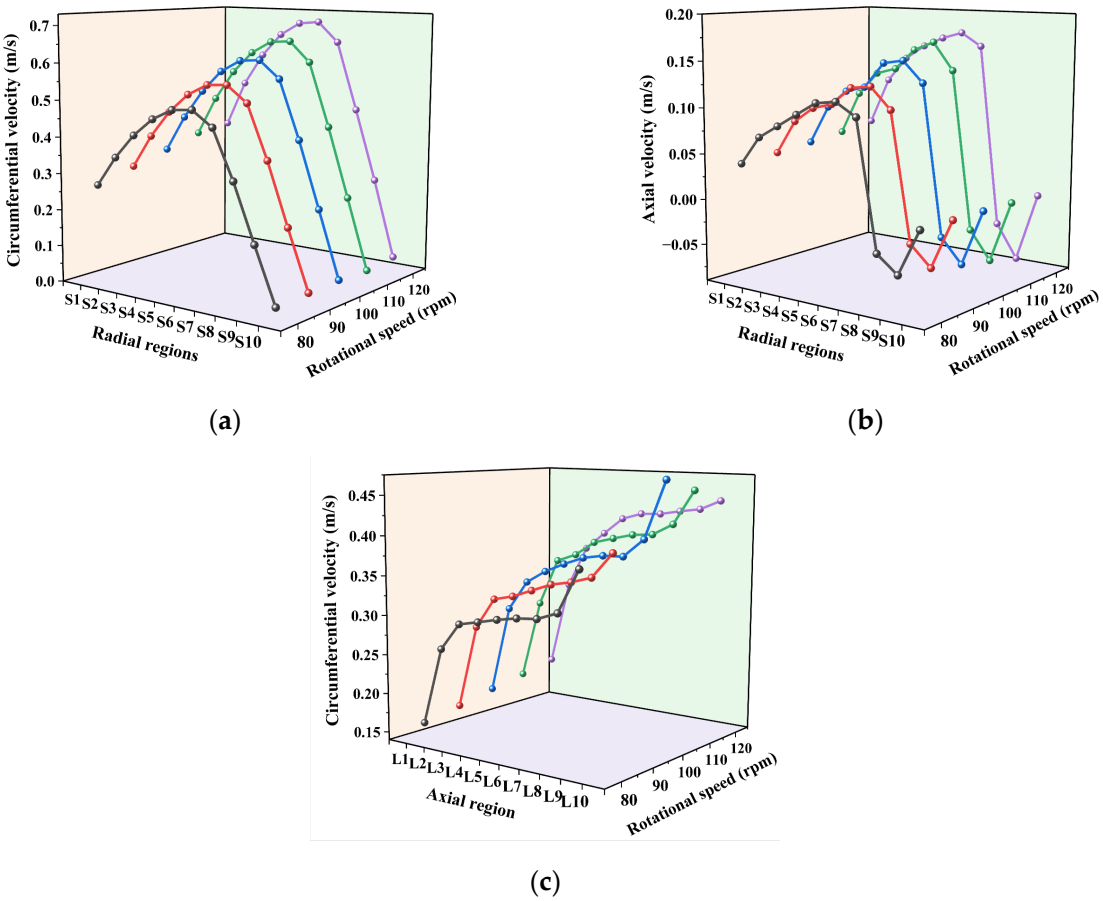


Figure 7. Effects of rotational speed on media kinematics: (**a**) Radial distribution of circumferential velocity; (**b**) Radial distribution of axial velocity; (**c**) Axial distribution of circumferential velocity.

The axial velocity of the grinding media remains positive throughout regions S_1–S_7 (the spiral region), as shown in Figure 7b, indicating stable upward movement driven by the spiral agitator. As the radial position increases, the axial velocity of the grinding media continuously rises, peaking at 0.078 m/s in the S6 region. This indicates that the maximum axial transport capacity occurs within this zone. In the circulation region (S_8–S_{10}), the axial velocity converges to negative values. Under the combined effects of gravity and centrifugal forces, the grinding media moves downward in this region, establishing a continuous recirculation pattern. In the peripheral zone of the spiral agitator, the grinding media experiences intense frictional interaction with the descending media from the adjacent circulation region. This results in a weakened upward velocity and consequently causes the peak axial velocity location to shift inward. Conversely, the media in the S_7 region is subjected to strong friction from the ascending media flow, leading to a reduction in its downward velocity. As the outermost part of the annular region is far from the blade tip, the circulatory flow there is relatively weak, resulting in an approximately U-shaped axial velocity profile in this zone. When the rotational speed increases from 80 to 120 rpm, with an overall improvement is observed across all regions. This enhancement in circulation effectively prevents the grinding media from accumulating at the mill bottom, thereby improving the overall grinding efficiency.

The rotational speed exerts a notable influence on the circumferential velocity of the grinding media across different axial regions, as shown in Figure 7c. The gap between the spiral agitator and the mill bottom, in the L_1 region, i.e., the grinding media, not being directly driven by the spiral agitator, exhibit a very low circumferential velocity of 0.16 m/s. This results in weak shear and compressive forces, leading to poor grinding performance. While the spiral agitator induces a sharp rise in circumferential velocity, the growth rate progressively slows as the grinding media advances through the L_3–L_8 regions. Meanwhile, the pressure on the media in the upper region decreases, with increasing axial height, while the circumferential velocity rises. This enhancement intensifies the shear forces acting on the grinding media, leading to progressively more effective grinding performance.

The circumferential velocity exhibits systematic enhancement across all axial regions, with the rotational speed increases. Notably, the media layer height shows a positive correlation with rotational speed. Under 80–90 rpm conditions, the peak media layer height is located in the L_9 region, where the radial distribution gradient significantly steepens, and the circumferential velocity driven by the spiral agitator reaches its maximum. When rotational speed reaches 100–120 rpm, the media layer advances to the L_{10} region. The consequent increase in packing density intensifies media collisions and energy loss, ultimately producing a graded reduction in circumferential velocity.

Every media layer shows positive axial velocity within the spiral region while displaying negative values in the circulation region, along the axial direction. The circulation behaviour of grinding media cannot be accurately represented by layer-averaged axial velocity measurements. Therefore, this study does not consider the axial velocity along the axial direction.

The grinding media exhibits distinct dynamic characteristics in different regions of the mill chamber. The variation in the total media–media collision frequency and the total media–media energy as a variation in the rotational speed, as shown in Figure 8a. As the rotational speed increases from 80 to 120 rpm, the frequency of media collisions decreases from 68,178 to 59,104, while the total media–media energy increases from 90.0 J to 106.7 J. Rather than simply increasing the velocity and collision frequency of the media, a higher rotational speed forces the media toward the mill shell via centrifugal force, causing them to follow a collective revolution. This motion thereby reduces relative movement, random sliding, and consequently, the effective collision probability among the particles within the media mass. Compared with high-speed operation, the media bed is more densely packed at low rotational speeds, resulting in frequent inter-media sliding. This motion generates numerous low-energy collisions, which reduce the overall collision intensity and thereby lead to inferior grinding performance.

The effect of rotational speed on energy dissipation during media–media and media–agitator interactions, as shown in Figure 8b. The analysis indicates that as the rotational speed increases from 80 to 120 rpm, the media–media energy loss rises from 2.6 J to 3.71 J, while the media–impeller energy loss increases from 3.16 J to 4.5 J, both exhibiting a significant upward trend. An increase in rotational speed enhances the total energy and circumferential velocity of the grinding media. This intensifies both media–media and media–impeller collisions and friction, thereby elevating the energy dissipation. It is particularly noteworthy that the energy loss at the media–spiral agitator interface is consistently higher than that at the media–media interface, suggesting that the interaction between the spiral agitator and the media serves as the primary source of energy dissipation.

The collision frequency of grinding media decreases across all radial regions with increasing rotational speed, as shown in Figure 8c, which aligns with the overall trend observed in Figure 8a. However, the S_{10} zone exhibits an increase in collision frequency. This is because the increased rotational speed enhances the centrifugal force on the media,

thereby driving them toward the mill wall. As shown in Figure 8c, an increase in the rotational speed of the spiral agitator raises the circumferential velocity of the media across all regions. Although this leads to a decline in collision frequency, it results in a more substantial increase in the average effective energy between media. The SP_6 region exhibits the maximum average effective energy between media, which corresponds to its optimal grinding performance. As confirmed by Figure 6a, this trend ultimately results in a net increase in average effective energy between media across all regions [22].

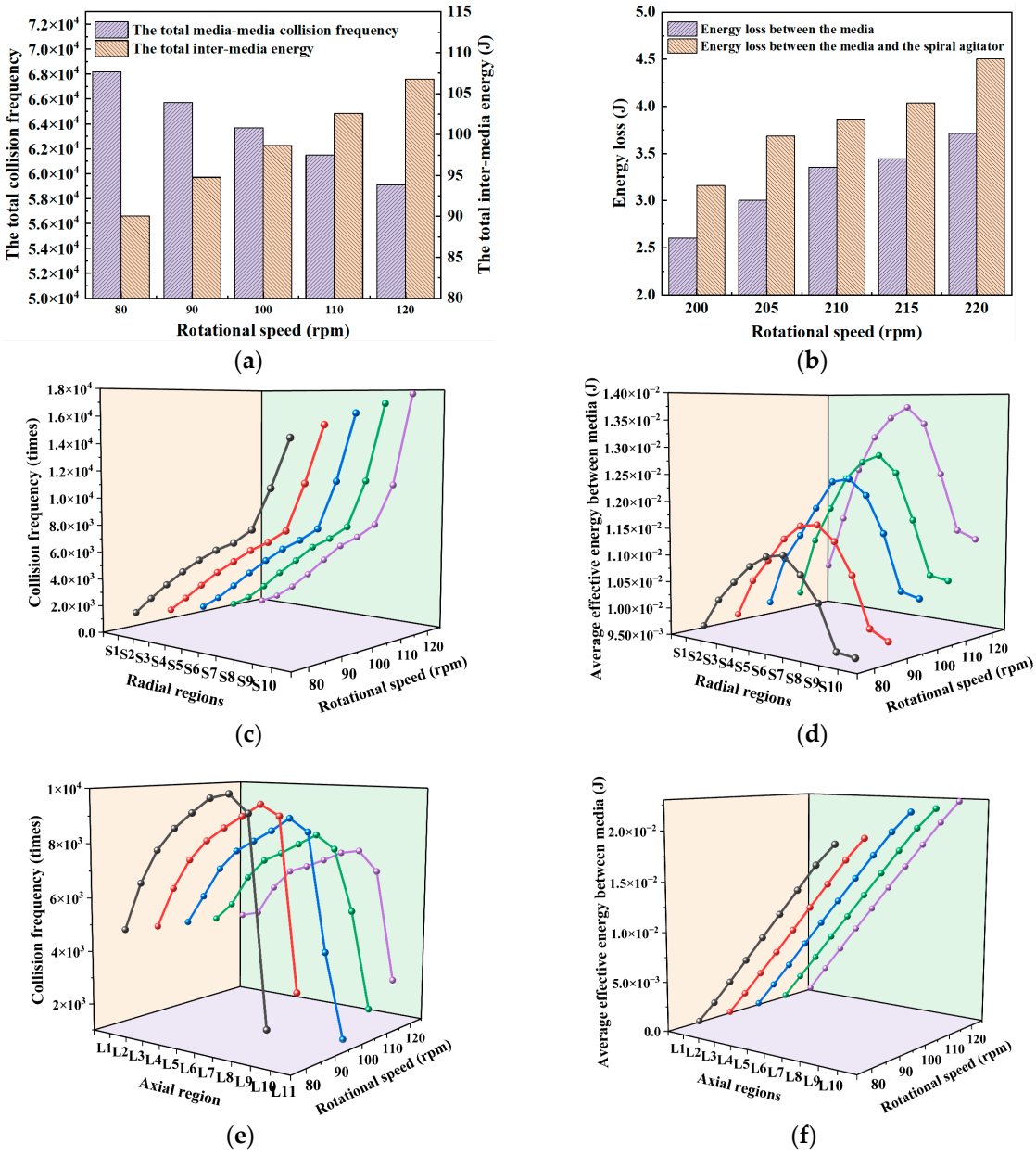


Figure 8. Influence of rotational speed on the dynamic characteristics of the media. (**a**) Total media collision count and total media–media energy; (**b**) Energy loss; (**c**) Collision frequency in radial regions; (**d**) Average effective media–media energy in radial regions; (**e**) Collision frequency in axial regions; (**f**) Average effective media–media energy in axial regions.

The collision frequency of the grinding media progressively increases along the axial direction, as shown in Figure 8e. In contrast, across regions L_1 to L_8, the collision frequency at 120 rpm is significantly lower than that at 80 rpm. The motion height of the media bed increases with rotational speed. Specifically, at 80 and 90 rpm, the media bed height reaches zone L_9, while at speeds between 100 and 120 rpm, it extends to zone L_{10}. Consequently, the elevated bed height increases the number of grinding media within these zones, which in turn raises the inter-media collision frequency. The average effective energy between media exhibits a consistent but slightly increasing trend along the axial direction under different rotational speeds, as shown in Figure 8f. The average effective energy between media peaks in the upper region of the media bed along the axial direction, indicating optimal grinding performance in this zone. Due to the insignificant influence of various operational factors on this axial energy distribution, further analysis is excluded from the subsequent discussion.

3.2. Effect of Diameter on Media Kinematics and Dynamics

The influence of the spiral agitator diameter on the motion characteristics of the grinding media is shown in Figure 9. The circumferential velocity of the media peaks in region S_5 for most diameters, in Figure 9a. The exceptions are the 220 mm and 215 mm diameters, for which the peak occurs in region S_6. In all cases, the maximum velocity is located within the peripheral region of the spiral agitator. As the diameter increases from 200 mm to 220 mm, the circumferential velocity of the media rises across all regions. This increase is most pronounced in the S_7 region and is accompanied by a broadening of the effective grinding zone [15].

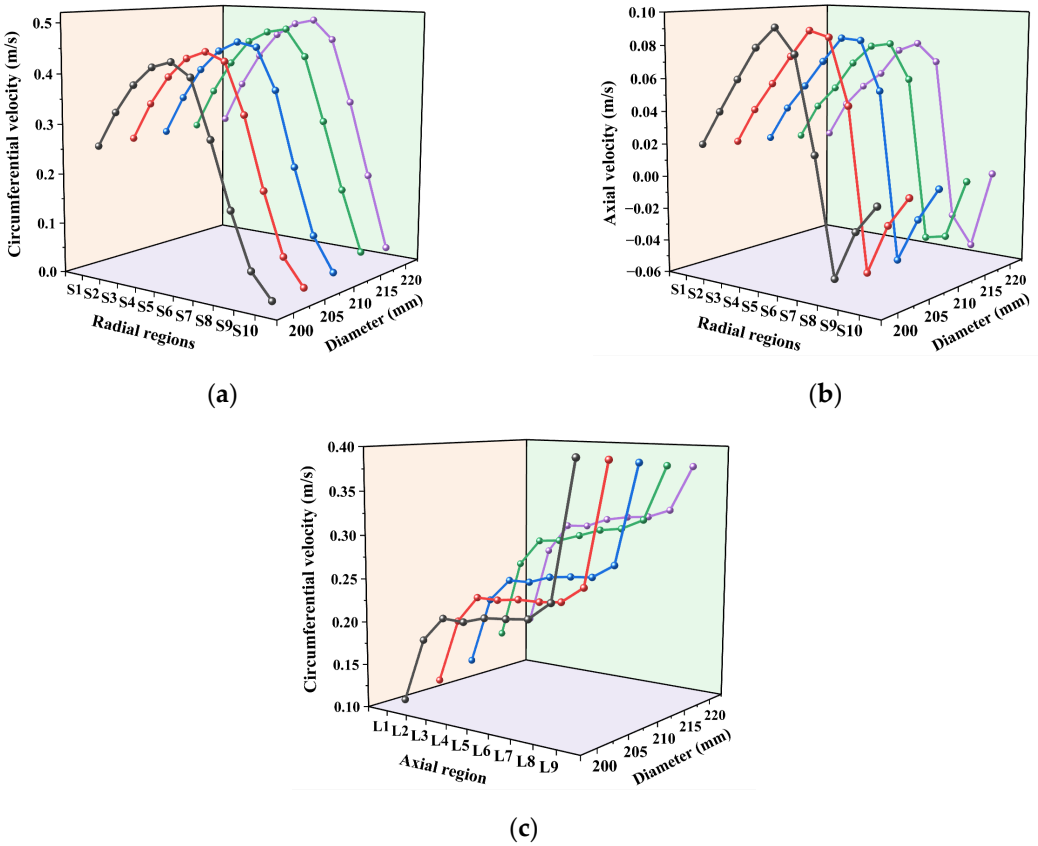


Figure 9. Effects of diameter on media kinematics: (**a**) Radial distribution of circumferential velocity; (**b**) Radial distribution of axial velocity; (**c**) Axial distribution of circumferential velocity.

The axial velocity in the spiral region decreases as the spiral agitator diameter increases, accompanied by a reduction and outward shift of the maximum axial velocity, as shown in Figure 9b. In the recirculation zone, the axial velocity of the media increases significantly. This is because a larger agitator diameter expands the spiral region, thereby increasing the amount of media conveyed upward. This upward movement, in turn, reduces the media frequency at the mill bottom, which prompts the media in the annular region to rapidly flow into the bottom region.

The spiral agitator diameter exerts notable control over the circumferential velocity distribution along the axial direction in the grinding system, as illustrated in Figure 9c. The velocities achieved with larger agitator diameters are significantly higher than those with smaller diameters. This can be primarily attributed to the larger diameter, which provides broader radial coverage and enhanced kinetic energy transfer efficiency to the media.

A further analysis of the influence of diameter on the circumferential velocity gradient reveals that in regions L_1 to L_8, the media velocity corresponding to a 220 mm diameter is significantly higher than that of a 200 mm diameter. This enhancement stems from the larger agitator's greater capability to regulate the axial distribution of media and its more intense shear action. Although the circumferential velocity of the media reaches its peak in the L_9 region for all spiral agitators, the velocity gradient corresponding to the 220 mm diameter is slightly lower than that of the 200 mm diameter. This phenomenon is linked to the increased media packing density in the top region resulting from the larger diameter. This increase in density elevates the media–media collision frequency, which in turn leads to greater kinetic energy dissipation and consequently, a decrease in circumferential velocity.

The total number of collisions and total energy between grinding media as a variation in the spiral agitator diameter is illustrated in Figure 10a. Within the diameter range of 200 mm to 210 mm, the frequency of media collisions shows little variation. In contrast, the frequency reaches a maximum of 70,907 at a diameter of 215 mm. Furthermore, the total media–media energy exhibits a continuous increase from 84.7 J to 90.1 J with increasing diameter. This improvement is attributed to the larger-diameter spiral agitator, which exerts kinetic energy over a broader radial range, achieves higher energy transfer efficiency, and thereby delivers superior grinding performance.

The effect of the spiral agitator diameter on energy dissipation during both media–media and media–agitator interactions is illustrated in Figure 10b. The analysis indicates that as the diameter increases from 200 mm to 220 mm, both energy losses reach their maximum values at a diameter of 215 mm, peaking at 3.57 J and 3.15 J, respectively. While an increase in diameter expands the effective grinding zone, it also intensifies media–media and media–impeller collisions and friction, consequently leading to elevated energy dissipation, consequently, the grinding efficiency is improved.

Variations in the spiral agitator diameter exhibit minimal effect on the collision frequency of the grinding media, as shown in Figure 10c. The average effective energy between media between grinding media across different regions, exhibits a consistent trend under various rotational speeds. As shown in Figure 10d, an increase in diameter expands the effective grinding zone and shifts the peak average effective energy between media outward radially. Meanwhile, the average effective energy between media rises in all regions, with a maximum increase of 0.00109 J.

The variation in axial collision frequency of the grinding media across regions L_1 to L_9 under different diameters, as shown in Figure 10e. All curves demonstrate a consistent trend of an initial increase followed by a decrease. The frequency of collisions gradually increases from region L_1 to L_7, where it peaks, before decreasing sharply from L_7 to L_9.

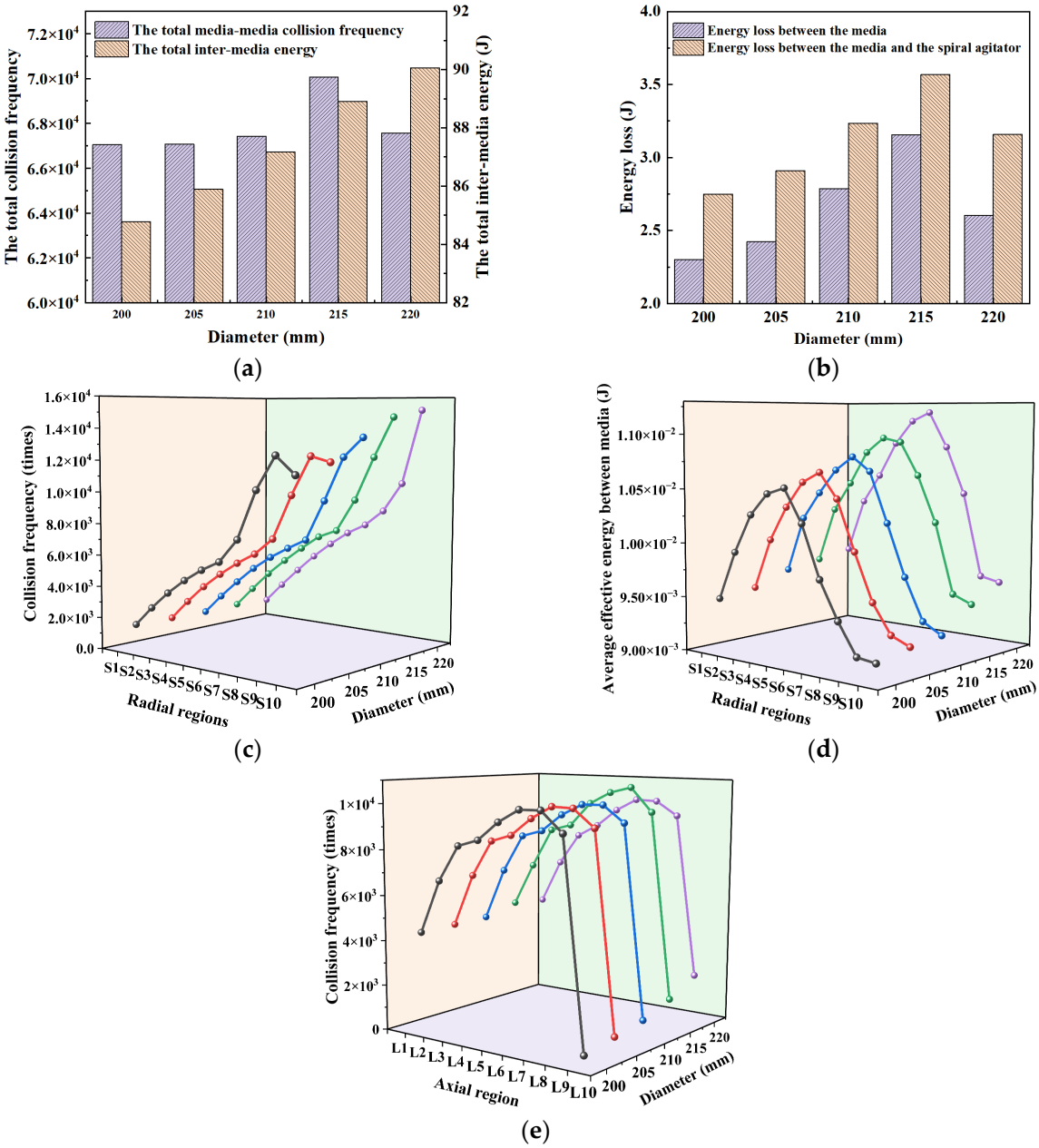


Figure 10. Influence of diameter on the dynamic characteristics of the media. (**a**) Total media collision count and total media–media energy; (**b**) Energy loss; (**c**) Collision frequency in radial regions; (**d**) Average effective media–media energy in radial regions; (**e**) Collision frequency in axial regions.

3.3. Effect of Pitch on Media Kinematics and Dynamics

The influence of the pitch on the motion state of the grinding media is shown in Figure 11. The circumferential velocity of the grinding media remains virtually unchanged across all regions when the pitch increases from 150 mm to 190 mm, as shown in Figure 11a, indicating a negligible effect of pitch on this parameter. The helix angle of the spiral agitator shows a progressive increase with rising pitch. This geometry enhances the axial component of the force imparted to the media during rotation, as evidenced in Figure 11b, thereby increasing the axial velocity across all regions from S_1 to S_{14}. However, the increase remains marginal, with a maximum value of 0.02 m/s.

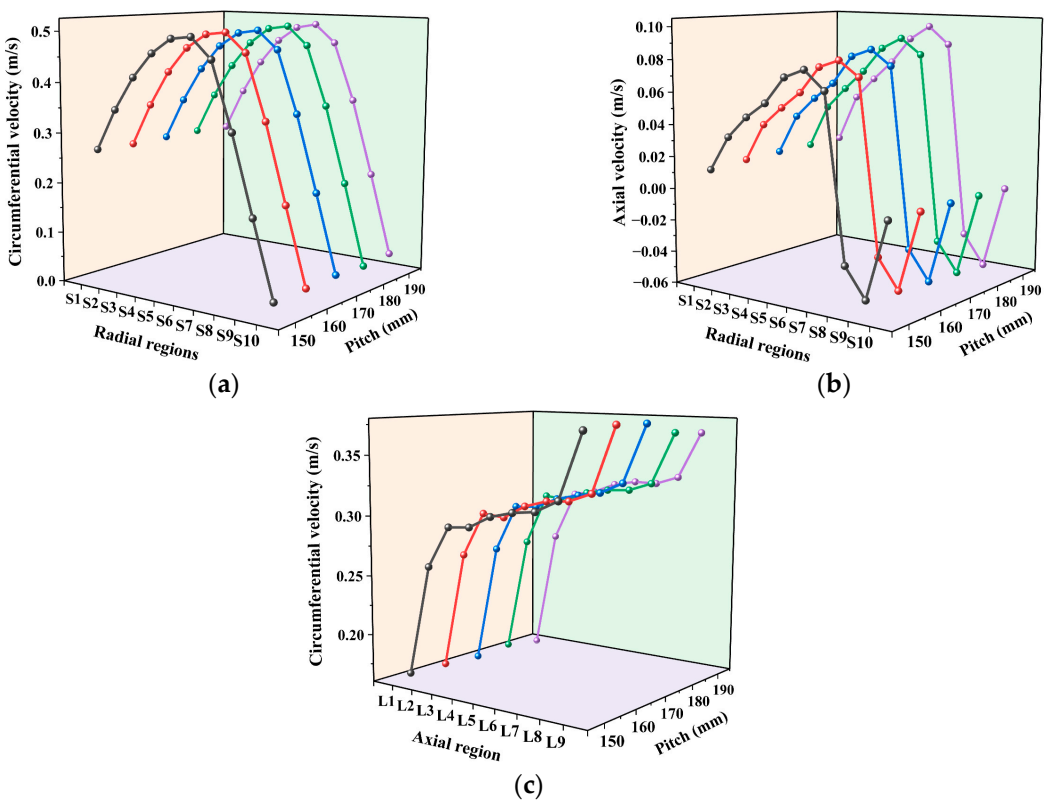


Figure 11. Effects of pitch on media kinematics: (**a**) Radial distribution of circumferential velocity; (**b**) Radial distribution of axial velocity; (**c**) Axial distribution of circumferential velocity.

The agitator pitch exerts limited influence on the circumferential velocity of the media across axial regions, in grinding systems driven by a spiral agitator, as shown in Figure 11c. Globally, the curves under all pitch conditions exhibit a consistent trend: a rapid initial rise, followed by a slow growth phase, and culminating in a second accelerated rise. This trend indicates that the influence of the pitch on the circumferential velocity of the grinding media strengthens progressively with increasing axial region. It is noteworthy that in the top L_9 region, the media packing density increases with the pitch, which in turn suppresses the circumferential velocity, resulting in a decreasing trend.

The total number of collisions and total energy between grinding media is illustrated in Figure 12a, as a variation in the pitch. Both the total media–media collision frequency and the total media–media energy exhibit a consistent yet modest increase with increasing pitch. This is attributed to the increased axial velocity of the media at a higher pitch, which enhances the overall circulation within the mill. Specifically, as the pitch increases from 150 mm to 190 mm, the collision frequency rises by 5988, and the total energy grows by 4.74 J.

The effect of the pitch on energy dissipation during both media–media and media–agitator interactions is illustrated in Figure 12b. The analysis indicates that as the pitch increases from 150 mm to 190 mm, the media–media energy loss rises from 2.6 J to 3.05 J, while the media–agitator energy loss increases from 3.16 J to 3.68 J, both exhibiting a marked upward trend. An increase in the pitch enhances the axial lifting force on the media, thereby intensifying both media–media collisions and media–agitator friction, which consequently leads to elevated energy dissipation.

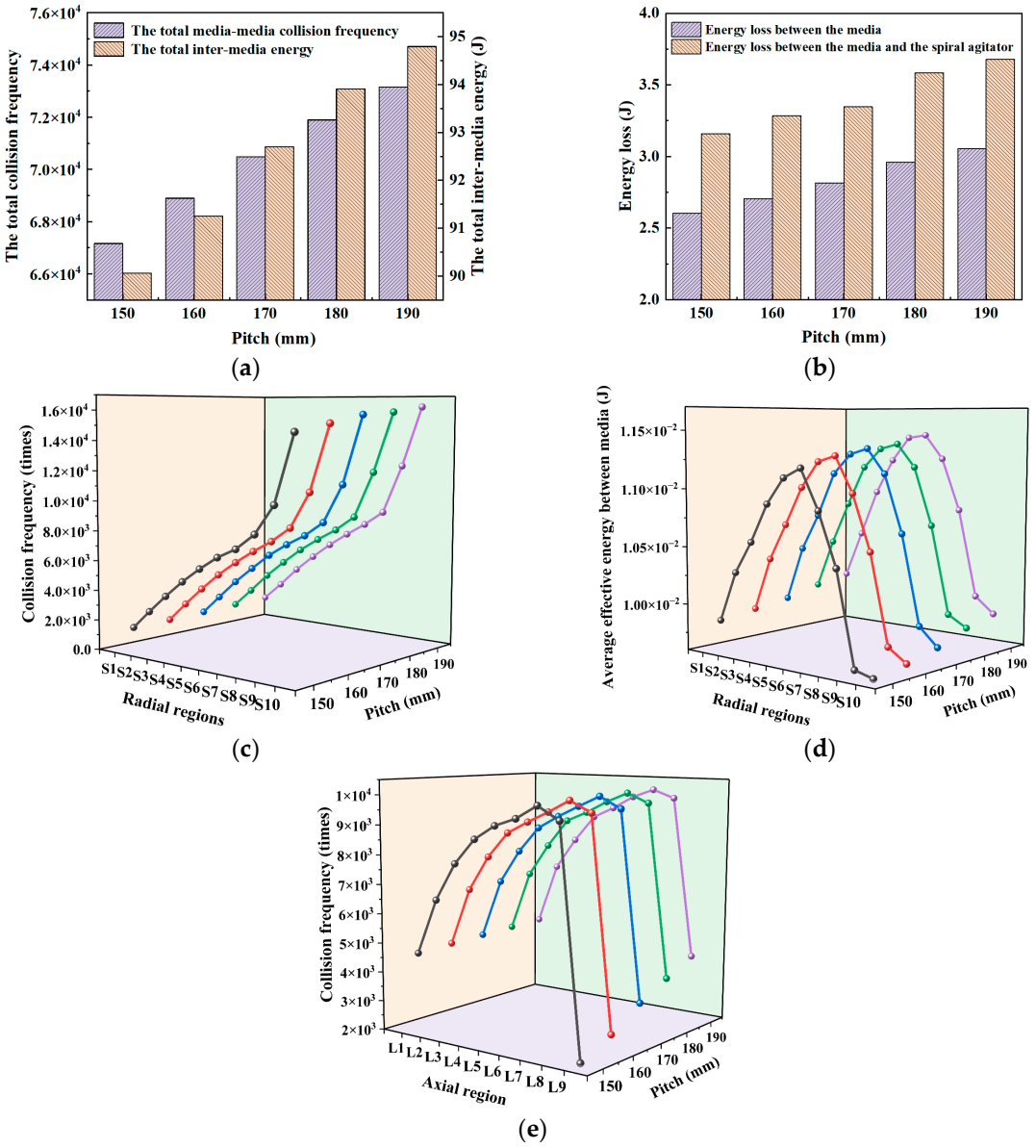


Figure 12. Influence of pitch on the dynamic characteristics of the media. (**a**) Total media collision count and total media–media energy; (**b**) Energy loss; (**c**) Collision frequency in radial regions; (**d**) Average effective media–media energy in radial regions; (**e**) Collision frequency in axial regions.

Both the frequency of media collisions and the average effective energy between media exhibit a consistent trend across all regions under different pitch conditions, as shown in Figure 12c,d. The collision frequency increases slowly across regions S_1 to S_8, accelerates through S_8–S_{10}, and reaches its maximum value in region S_{10}. The average effective energy between media increases continuously through regions S_1–S_6, reaching its maximum in the spiral agitator zone. This peak location aligns with the region of maximum circumferential velocity, the grinding efficiency shows a concurrent improvement across all regions from S_1–S_6, after which the energy decreases rapidly in the recirculation zone.

The collision frequency curves corresponding to all spiral agitator pitch values exhibit a consistent pattern of initially increasing and then decreasing with rising axial position, as shown in Figure 12e. Specifically, the collision frequency progressively increases from region L_1 to L_7, peaking in L_7, followed by a rapid decrease from L_7 to L_9. As the pitch increases, the collision frequency rises across all regions, with the most pronounced increase of 2251 occurrences observed in the L_9 zone.

3.4. Effect of Filling Level on Media Kinematics and Dynamics

The influence of the filling level on the motion state of the grinding media is shown in Figure 13. The circumferential velocity of the media shows little variation with the media filling level, as shown in Figure 13a,b [43]. All conditions exhibit an identical velocity profile, reaching a maximum of 0.495m/s in the S_6 region. A corresponding trend is observed for the axial velocity, which reaches its maximum value of 0.078m/s in the S_6 region.

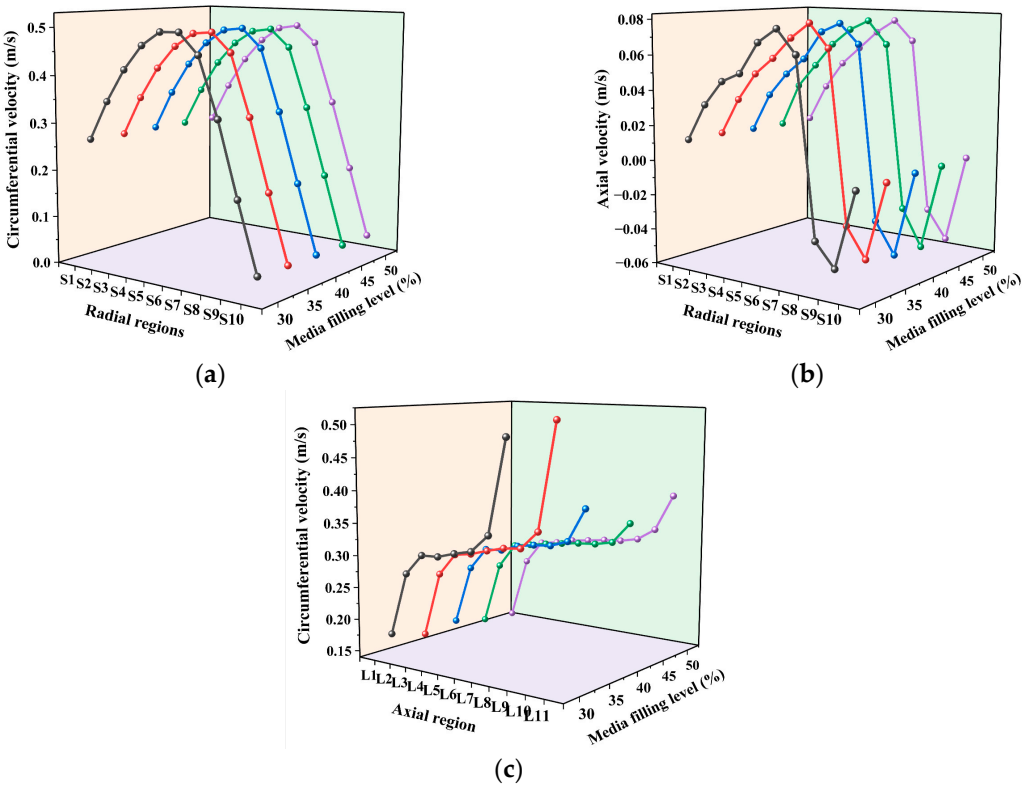


Figure 13. Effects of media filling level on media kinematics: (**a**) Radial distribution of circumferential velocity; (**b**) Radial distribution of axial velocity; (**c**) Axial distribution of circumferential velocity.

The variation in the circumferential velocity along the axial direction under different filling levels is shown in Figure 13c. Overall, all filling level curves follow a typical three-stage trend: an initial rapid rise, followed by a period of slow growth, and a final accelerated rise. The circumferential velocity of media with a high filling level is lower than that with a low filling level. Furthermore, different filling levels result in varying Motion heights. When the media reach the top layer, their circumferential velocity surges dramatically due to the low media density in this zone. When the media move to the uppermost layer, the frequency of media in this region is small, resulting in a sharp increase in circumferential velocity.

The total number of collisions and total energy between grinding media as a variation in the filling level, as illustrated in Figure 14a. Both the total frequency of media–media collisions and the total media–media energy show a continuous increase with the media filling level. The collision frequency rises from 54,726 to 90,891, while the total energy increases from 58.24 J to 141.33 J. This can be primarily attributed to the increased number of grinding media set in motion by the impeller at higher fill levels. This leads to a rise in both inter-media collision frequency and total energy. Furthermore, a higher fill level is typically associated with greater throughput.

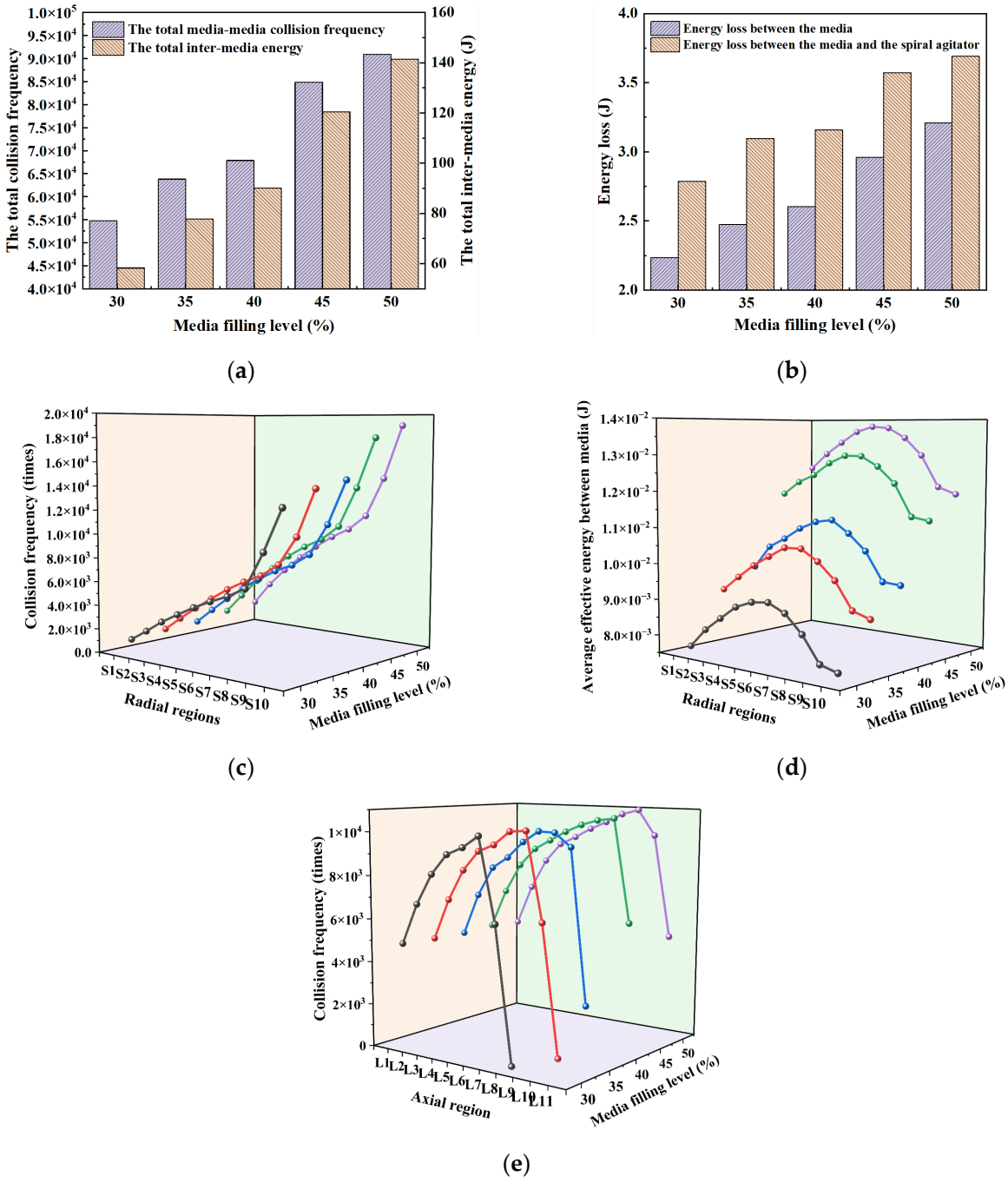


Figure 14. Influence of media filling level on the dynamic characteristics of the media. (**a**) Total media collision count and total media–media energy; (**b**) Energy loss; (**c**) Collision frequency in radial regions; (**d**) Average effective media–media energy in radial regions; (**e**) Collision frequency in axial regions.

The effect of the filling level on energy dissipation during both media–media and media–agitator interactions is illustrated in Figure 14b. The analysis indicates that as the media filling level increases from 30% to 50%, the media–media energy loss rises from 2.23 J to 3.21 J, while the media–agitator energy loss increases from 2.79 J to 3.69 J, both exhibiting a marked upward trend. Elevated energy dissipation results from the increased media frequency at higher filling levels, which enhances media–media collisions and media–agitator friction. Hence, judicious control of the filling level is key to achieving lower energy consumption and superior grinding effectiveness. The pursuit of higher throughput, however, is often accompanied by increased energy loss.

Both the frequency of media collisions and the average effective energy between media exhibit a consistent trend across all regions under different filling level conditions, as shown in Figure 14c,d. Under a high media filling level, the mill contains a greater frequency of media, which increases the collision frequency and elevates the media bed to a greater height via the spiral agitator. These factors collectively result in a significant enhancement of the average effective energy between media.

The collision frequency between grinding media exhibits a consistent increasing trend with rising axial position under all filling levels, as shown in Figure 14e. Moreover, there is minimal variation in the collision frequency across the different filling level curves within each specific region. At a 30% media filling level, the frequency of media in the L_7 and L_8 regions decreases noticeably, consequently leading to a sharp drop in collision frequency. A similar pattern is observed under other filling level conditions.

4. Conclusions

This investigation focuses on the kinematic and dynamic behaviour of grinding media in a vertical spiral agitator mill under wet conditions, systematically analysing the effects of various factors on the distribution of media velocity in circumferential, axial, as well as on collision frequency, effective energy between media, and energy loss patterns. The principal conclusions are as follows.

The greater the velocity difference between the media, the stronger the resulting shear force, which enhances fine grinding efficiency. The circumferential velocity of the grinding media and the average effective energy between media increase along the radial direction, both peaking in the SP6 region. This indicates that the grinding efficiency is highest in this specific zone. The circumferential velocity of the media exhibits a characteristic three-zone pattern along the axial direction. In the top region of the media bed, both the circumferential velocity and the average inter-media effective energy reach their maxima, indicating the most effective grinding performance in this zone. The kinematic and dynamic properties of the grinding media are significantly influenced by rotational speed, followed by diameter, while the effects of fill level and pitch lead are minimal.

The total collision frequency and energy of the grinding media are highly sensitive to variations in rotational speed and filling level. Specifically, increasing the rotational speed from 80 to 120 rpm reduces the collision frequency by 9074 but raises the total energy by 16.7 J. Although the total media–media energy shows a continuous increase, energy dissipation is also intensified. The rotational speed contributes most significantly to this dissipation, elevating media–media energy loss by 1.11 J and media–agitator energy loss by 1.34 J.

Similarly, the effects of various parameters on the inter-media collision frequency and average effective energy across radial regions correspond with their effects on the total collision frequency and total energy. Moreover, along the axial direction, the rotational speed exerts the most significant influence on these two parameters in all regions. The highest average effective energy occurs at the top of the material bed, indicating more efficient grinding performance in this zone.

Author Contributions: Conceptualization, R.G. and W.W.; Software, W.W. and Z.Q.; Formal analysis, R.G., W.W., S.Z. and Z.M.; Data curation, W.W., S.Z. and Z.Q.; Writing—original draft, W.W.; Writing—review & editing, R.G., S.Z., Z.M., Q.W. and Z.Q.; Visualization, R.G., Q.W. and Y.W.; Supervision, R.G. and Y.W.; Funding acquisition, R.G. All authors have read and agreed to the published version of the manuscript.

Funding: This work was supported by a grant from the Henan Provincial Department of Science and Technology (241100220300-4-1), Henan Science and Technology Projects (No.: 252102220058), and Key Scientific Research Project of Colleges and Universities in Henan Province (No.: 26A590001).

Data Availability Statement: The data that support the findings of this study are available from the corresponding author upon reasonable request.

Acknowledgments: Sincere gratitude is extended for the joint funding support provided to this research by the Henan Provincial Department of Science and Technology (241100220300-4-1), Henan Science and Technology Projects (No.: 252102220058), and Key Scientific Research Project of Colleges and Universities in Henan Province (No.: 26A590001).

Conflicts of Interest: The authors declare that they have no known competing financial interests or personal relationships that could have appeared to influence the work reported in this paper.

References

1. De Carvalho, R.M.; Oliveira, A.L.R.; Petit, H.A.; Tavares, L.M. Comparing Modeling Approaches in Simulating a Continuous Pilot-Scale Wet Vertical Stirred Mill Using PBM-DEM-CFD. *Adv. Powder Technol.* **2023**, *34*, 104135. [CrossRef]
2. Wu, C.; Chen, Z.; Liao, N.; Zeng, C.; Wang, Y.; Tian, J. Enhancing the Grinding Efficiency of a Magnetite Second-Stage Mill through Ceramic Ball Optimization: From Laboratory to Industrial Applications. *Minerals* **2024**, *14*, 160. [CrossRef]
3. Shi, F.; Morrison, R.; Cervellin, A.; Burns, F.; Musa, F. Comparison of Energy Efficiency between Ball Mills and Stirred Mills in Coarse Grinding. *Miner. Eng.* **2009**, *22*, 673–680. [CrossRef]
4. Xiao, X.; Zhang, G.; Feng, Q.; Xiao, S.; Huang, L.; Zhao, X.; Li, Z. The Liberation Effect of Magnetite Fine Ground by Vertical Stirred Mill and Ball Mill. *Miner. Eng.* **2012**, *34*, 63–69. [CrossRef]
5. Cao, K.; Li, X.H.; Gao, H.D.; Zhang, L.X.; You, F. Design and Analysis of a Vertical Screw Stirring Device for Feeding Dairy Goats. *Int. J. Simul. Model.* **2023**, *22*, 462–473. [CrossRef]
6. Esteves, P.M.; Mazzinghy, D.B.; Galéry, R.; Machado, L.C.R. Industrial Vertical Stirred Mills Screw Liner Wear Profile Compared to Discrete Element Method Simulations. *Minerals* **2021**, *11*, 397. [CrossRef]
7. Höfels, C.; Dambach, R.; Kwade, A. Geometry Influence on Optimized Operation of a Dry Agitator Bead Mill. *Miner. Eng.* **2021**, *171*, 107050. [CrossRef]
8. Zafar, U.; Vivacqua, V.; Calvert, G.; Ghadiri, M.; Cleaver, J.A.S. A Review of Bulk Powder Caking. *Powder Technol.* **2017**, *313*, 389–401. [CrossRef]
9. Can, M.; Altun, O. Performance Comparison of the Vertical and Horizontal Oriented Stirred Mill: Pilot Scale IsaMill vs. Full-Scale HIGMill. *Minerals* **2023**, *13*, 315. [CrossRef]
10. Guo, Y.; Curtis, J.S. Discrete Element Method Simulations for Complex Granular Flows. *Annu. Rev. Fluid Mech.* **2015**, *47*, 21–46. [CrossRef]
11. Kim, S.; Choi, W.S. Analysis of Ball Movement for Research of Grinding Mechanism of a Stirred Ball Mill with 3D Discrete Element Method. *Korean J. Chem. Eng.* **2008**, *25*, 585–592. [CrossRef]
12. Bian, X.; Wang, G.; Wang, H.; Wang, S.; Lv, W. Effect of Lifters and Mill Speed on Particle Behaviour, Torque, and Power Consumption of a Tumbling Ball Mill: Experimental Study and DEM Simulation. *Miner. Eng.* **2017**, *105*, 22–35. [CrossRef]
13. Fukui, S.; Tsunazawa, Y.; Hisatomi, S.; Granata, G.; Tokoro, C.; Okuyama, K.; Iwamoto, M.; Sekine, Y. Effect of Agitator Shaft Direction on Grinding Performance in Media Stirred Mill: Investigation Using DEM Simulation. *Mater. Trans.* **2018**, *59*, 488–493. [CrossRef]
14. Osborne, T.; Rhymer, D.; Werner, D.; Ingram, A.; Windows-Yule, C.R.K. Investigating the Impact of Impeller Geometry for a Stirred Mill Using the Discrete Element Method: Effect of Pin Number and Thickness. *Powder Technol.* **2023**, *428*, 118810. [CrossRef]
15. Daraio, D.; Villoria, J.; Ingram, A.; Alexiadis, A.; Stitt, E.H.; Marigo, M. Investigating Grinding Media Dynamics inside a Vertical Stirred Mill Using the Discrete Element Method: Effect of Impeller Arm Length. *Powder Technol.* **2020**, *364*, 1049–1061. [CrossRef]
16. Rhymer, D.; Ingram, A.; Sadler, K.; Windows-Yule, C.R.K. A Discrete Element Method Investigation within Vertical Stirred Milling: Changing the Grinding Media Restitution and Sliding Friction Coefficients. *Powder Technol.* **2022**, *410*, 117825. [CrossRef]
17. Rhymer, D.; Ingram, A.; Sadler, K.; Windows-Yule, C.R.K. Segregation in Binary and Polydisperse Stirred Media Mills and Its Role on Grinding Effectiveness. *Powder Technol.* **2024**, *443*, 119921. [CrossRef]
18. Wang, H.; Chen, R.; Li, D.; Zeng, Q.; Wen, X.; Lv, J.; Yan, X.; Ran, J.; Zhang, H. Flow Field Analysis and Engineering Application of the Turbulence-Forced Pulp Conditioner. *Physicochem. Probl. Miner. Process.* **2025**, *61*, 210645. [CrossRef]
19. Ma, H.; Zhou, L.; Liu, Z.; Chen, M.; Xia, X.; Zhao, Y. A Review of Recent Development for the CFD-DEM Investigations of Non-Spherical Particles. *Powder Technol.* **2022**, *412*, 117972. [CrossRef]

20. Bi, Z.; Zheng, L.; Li, T.; Zhang, B.; Ji, H.; Zhao, Z. Multi Factor Analysis of the Vertical Roller Mill Separator Based on BP Neural Network—Response Surface Joint Modeling. *Physicochem. Probl. Miner. Process.* **2025**, *61*, 208769. [CrossRef]
21. Fragnière, G.; Naumann, A.; Schrader, M.; Kwade, A.; Schilde, C. Grinding Media Motion and Collisions in Different Zones of Stirred Media Mills. *Minerals* **2021**, *11*, 185. [CrossRef]
22. Ji, H.; Wang, Z.; Qu, T.; Song, X.; Tang, B.; Li, Y.; Ma, L. Grinding Mechanism of Wet Vertical Spiral Stirred Mill Based on DEM-CFD: Role of Grinding Sphere Motion. *Particuology* **2025**, *103*, 151–163. [CrossRef]
23. Ford, E.; Naude, N. Investigating the Effect on Power Draw and Grinding Performance When Adding a Shell Liner to a Vertical Fluidised Stirred Media Mill. *Miner. Eng.* **2021**, *160*, 106698. [CrossRef]
24. Larsson, S.; Rodríguez Prieto, J.M.; Heiskari, H.; Jonsén, P. A Novel Particle-Based Approach for Modeling a Wet Vertical Stirred Media Mill. *Minerals* **2021**, *11*, 55. [CrossRef]
25. Winardi, S.; Widiyastuti, W.; Septiani, E.L.; Nurtono, T. Simulation of Solid-Liquid Flows in a Stirred Bead Mill Based on Computational Fluid Dynamics (CFD). *Mater. Res. Express* **2018**, *5*, 054002. [CrossRef]
26. Jonsén, P.; Hammarberg, S.; Pålsson, B.I.; Lindkvist, G. Preliminary Validation of a New Way to Model Physical Interactions between Pulp, Charge and Mill Structure in Tumbling Mills. *Miner. Eng.* **2019**, *130*, 76–84. [CrossRef]
27. Jiménez-Herrera, N.; Barrios, G.K.P.; Tavares, L.M. Comparison of Breakage Models in DEM in Simulating Impact on Particle Beds. *Adv. Powder Technol.* **2018**, *29*, 692–706. [CrossRef]
28. Fragnière, G.; Beinert, S.; Overbeck, A.; Kampen, I.; Schilde, C.; Kwade, A. Predicting Effects of Operating Condition Variations on Breakage Rates in Stirred Media Mills. *Chem. Eng. Res. Des.* **2018**, *138*, 433–443. [CrossRef]
29. Oliveira, A.L.R.; Rodriguez, V.A.; De Carvalho, R.M.; Powell, M.S.; Tavares, L.M. Mechanistic Modeling and Simulation of a Batch Vertical Stirred Mill. *Miner. Eng.* **2020**, *156*, 106487. [CrossRef]
30. Li, Z.; Wang, Y.; Li, K.; Zhang, B.; Chen, H. CFD-DEM Modeling of Particle Dissolution Behavior in Stirred Tanks. *Powder Technol.* **2024**, *442*, 119894. [CrossRef]
31. Li, Y.; Li, D. Investigation of the Force Closure for Eulerian-Eulerian Simulations: A Validation Study of Nine Gas-Liquid Flow Cases. *arXiv* **2019**, arXiv:1906.01189.
32. Piredda, M.M.; Asinari, P. Lattice Boltzmann Framework for Multiphase Flows by Eulerian–Eulerian Navier–Stokes Equations. *Computation* **2025**, *13*, 164. [CrossRef]
33. Petit, H.A.; De Oliveira, A.L.R.; Tavares, L.M. Validation of a Rheology-Dependent PBM-DEM-CFD Simulation Model of a Continuous Vertical Stirred Mill Operating under Different Conditions. *Chem. Eng. Sci.* **2025**, *306*, 121260. [CrossRef]
34. Bhonsale, S.; Scott, L.; Ghadiri, M.; Van Impe, J. Numerical Simulation of Particle Dynamics in a Spiral Jet Mill via Coupled CFD-DEM. *Pharmaceutics* **2021**, *13*, 937. [CrossRef] [PubMed]
35. Gu, R.; Qin, Z.; Zhao, S.; Xing, H.; Chen, L.; Yang, F. Mechanical Characteristics of Roll Crushing of Ore Materials Based on Discrete Element Method. *Sci. Rep.* **2025**, *15*, 771. [CrossRef]
36. Huang, S.; Huang, J.; Guo, J.; Mo, Y. Study on Wear Properties of the Flow Parts in a Centrifugal Pump Based on EDEM–Fluent Coupling. *Processes* **2019**, *7*, 431. [CrossRef]
37. Ren, Y.; Zhao, L.; Mo, X.; Zheng, S.; Yang, Y. Coupled CFD-DEM Numerical Simulation of the Interaction of a Flow-Transported Rag with a Solid Cylinder. *Fluid Dyn. Mater. Process.* **2024**, *20*, 1593–1609. [CrossRef]
38. Biswas, R.; Durbin, P.A.; Medic, G. Development of an Elliptic Blending Lag $k-\omega$ Model. *Int. J. Heat Fluid Flow* **2019**, *76*, 26–39. [CrossRef]
39. Qu, T.; Ma, L.; Song, X.; Wang, Z.; Zhang, S.; Zhao, Y.; Ji, H. Coupling simulation methodand experiment of vertical stirring mill based on DEM–CFD. *Conserv. Util. Miner. Resour.* **2025**, *45*, 15–22.
40. Tang, B.; Cheng, B.; Song, X.; Ji, H.; Li, Y.; Wang, Z. Experimental Study on the Influence of Rotational Speed on Grinding Efficiency for the Vertical Stirred Mill. *Minerals* **2024**, *14*, 1208. [CrossRef]
41. Hou, Y. DEM Simulation and Analysis of Operating Parameters on Grinding Performance of a Vertical Stirred Media Mill. Master's Thesis, University of British Columbia, Vancouver, BC, Canada, 2014.
42. Jayasundara, C.T.; Yang, R.Y.; Yu, A.B.; Curry, D. Discrete Particle Simulation of Particle Flow in IsaMill—Effect of Grinding Medium Properties. *Chem. Eng. J.* **2008**, *135*, 103–112. [CrossRef]
43. Liu, Z.; Wang, S.; Li, Y.; Mao, Y.; Ding, H.; Wu, S.; Xie, P.; Huang, Q. Analysis of Grinding Media Motion Behavior in a Vertical Spiral Stirred Mill Based on Discrete Element Method. *Granul. Matter* **2025**, *27*, 87. [CrossRef]

Disclaimer/Publisher's Note: The statements, opinions and data contained in all publications are solely those of the individual author(s) and contributor(s) and not of MDPI and/or the editor(s). MDPI and/or the editor(s) disclaim responsibility for any injury to people or property resulting from any ideas, methods, instructions or products referred to in the content.